Enhanced ultrasensitive detection of ozone gas using reduced graphene oxide-incorporated LaFeO$_3$ nanospheres for environmental remediation process

S. Thirumalairajan[1] · K. Girija[2] · Valmor R. Mastelaro[3] · K. S. Subramanian[1]

Abstract

An efficient and facile benign approach to develop reduced graphene oxide (rGO) incorporated into perovskite LaFeO$_3$ nanostructure with excellent surface area to detect ultrasensitive Ozone (O$_3$) gas for environmental remediation has been demonstrated. The prepared rGO/LaFeO$_3$ nanocomposites have diameter in the range ~ 1 μm constituting nanospheres with average size ~ 50 nm. Phase purity and chemical composition of rGO/LaFeO$_3$ nanocomposites were revealed through XRD and XPS analysis. The ozone gas sensing performance of rGO/LaFeO$_3$ nanocomposites was investigated and found to exhibit excellent sensitivity, high selectivity, good response (20 and 31 s) and recovery time (39 and 31 s) for 80 ppb at 100 °C when compared to pure LaFeO$_3$ nanostructures. These results indicate that the composites of rGO not only enhanced the ozone gas sensing response at low ppb concentration, but also a decrease in the working temperature. From these perspectives, rGO/LaFeO$_3$ nanocomposites based ozone gas sensor can be regarded as a promising candidate for environmental remediation process in near future.

1 Introduction

Detection of toxic gases play a critical role in environment remediation process, because fast development in industries and passionate use of automobile have caused sever air pollution. The monitoring of toxic gases such as carbon monoxide (CO), nitrogen dioxide (NO$_2$), ammonia (NH$_3$) and ozone (O$_3$) etc., have attracted huge attention [1–3]. In particular, O$_3$ is the most common air pollutant produced and powerful oxidizing reagent, having continuing demand for its efficient detection not only for industrial safety concerns but also environment remediation [4, 5]. Those exposed to O$_3$ below 100 ppb for 3 h will sustain a 20% loss of breathing capacity and 1 ppm of O$_3$ for 6 h will suffer an attack of bronchitis. It was observed that a mouse exposed to 10 ppm of O$_3$ for 10 h did not survive as reported by World Health Organization, WHO [6]. Thus, the sensitivity and selectivity measurement of O$_3$ has dynamic importance for a pollutant-free ecosystem [7]. In this regard, intensive attention to develop new ozone gas sensor reliable at ppb level detection with fast response, recovery time and low operating temperature is required.

To meet these requirements, shape-dependent perovskite (ABO$_3$)/graphene oxide (GO) nanocomposite based toxic gas sensors have considerable interest, because it significantly enhances the catalytic properties. Reduced GO (rGO), an attractive carbon family member and allotrope of carbon have two-dimensional single atomic layers. It has unique structure with sp^2 hybridized carbon atoms. It shows remarkable properties such as good electrical conductivity, large surface area and fast charge carrier density. rGO plays an important role in adsorbing catalytic molecules, because rGO sheets desire to aggregate irreversibly, due to the stack of strong π–π interactions [8–10]. In addition, p-type semiconductors have distinct surface reactivity and oxygen adsorption capacity, which benefits the enhancement of gas sensing performance when incorporated with other components especially GO [8–10]. LaFeO$_3$, a p-type material with majority hole carriers have good oxidation–reduction characteristics at wide temperature due to its

✉ S. Thirumalairajan
  sthirumalairajan@gmail.com

[1] Department of Nano Science and Technology, Tamil Nadu Agricultural University, Coimbatore 641 003, India

[2] Department of Physics, Dr. N.G.P. College of Arts and Science, Coimbatore 641 048, India

[3] Instituto de Física de São Carlos (IFSC), University de São Paulo, CP 369, São Carlos, SP 13560-970, Brazil

high chemical stability for practical applications. In literature, several devices based on WO_3, SnO_2, ZnO, Ag_2WO_4, $CuAlO_2$ and $CuWO_4$ have been studied to detect the ozone level in the atmosphere. Nevertheless, these sensors were reported with a low or unknown selectivity [11–17]. In other perspective, researchers have demonstrated that rGO tends to conjugate with perovskite nanostructures under the wet chemical growth reaction and its sensing performance can be greatly improved due to the synergistic effect. Above-mentioned composites are used as gas sensors at operating temperatures ~ 200 to 450 °C [18–21]. But high temperature promotes the adsorption/desorption process of oxygen and increase the material response in the presence of reducing and oxidizing gases. Nevertheless, the decrease in the material working temperature is an important issue for fabrication of low power consumption and small size sensing devices. For example, Mishra et al. prepared SnO_2 quantum dots decorated on rGO and found a reversible response to H_2 and LPG at operating temperature of 250 °C [22]. Jinjin Shi et al. prepared the rGO/WO_3 nanosheet composite with a sensitivity of 19.8% for 100 ppb toxic gases at 330 °C [23]. However, to the best of our knowledge, the ozone gas sensing performance of $rGO/LaFeO_3$ nanocomposites have not been reported in the open literature.

In the present work, microsphere $LaFeO_3$ nanostructure and $rGO/LaFeO_3$ nanocomposites were prepared via facile and environment friendly process. The ppb trace level, selectivity and sensitivity of ozone gas at low temperature were studied. Incorporation of rGO with $LaFeO_3$ nanospheres help to achieve higher response, sensitivity and excellent selectivity. $rGO/LaFeO_3$ nanocomposite exposed outstanding enhancement in ozone sensing when compared with the pure $LaFeO_3$ nanostructure. An understanding of the influence of morphology, size, incorporation of rGO,

specific surface area and oxygen vacancies were helpful to enhance the gas sensing performance as discussed detail in sensing mechanism.

2 Experimental section

2.1 Synthesis of GO and rGO

All chemicals purchased were analytical pure grade (99.99%) and used without further purification. GO was synthesized using the modified Hummers method [24]. In this study, expandable graphite powder (2 g) was mixed into the mixture of concentrated H_2SO_4 and H_3PO_4. The mixture was then stirred for 30 min. Subsequently, $KMnO_4$ was added slowly to this solution under stirring at 35–40 °C. During the oxidation reaction, the color of the solution changed from dark black colour into brown. The solution was then heated to 50 °C and stirred further overnight to complete the oxidation of graphite.

For the synthesis of rGO by one-pot in situ hydrothermal method, 50 mg of as synthesized GO powder was dispersed into 50 ml of milli-Q water at 50 °C. The dispersed GO was then exfoliated under ultra-sonication treatment for 1 h and subsequently the solution was transferred into a 110 ml Teflon-lined stainless steel autoclave and heated at 180 °C overnight. The autoclave was then cooled to room temperature. The obtained precipitate was washed with milli-Q water and C_2H_5OH. The remaining material was then dried at 90 °C in an open-air oven. Finally, black powder of rGO was collected. The schematic illustration of the formation process has been presented in Fig. 1.
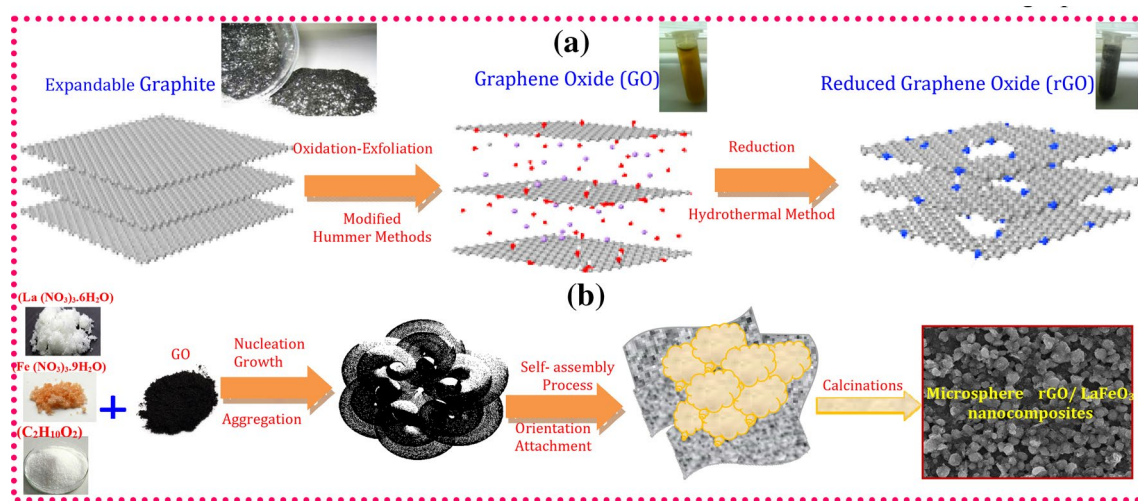

Fig. 1 Schematic diagram illustrating the preparation and growth mechanism of **a** GO into rGO and **b** microsphere $rGO/LaFeO_3$ nanocomposites

2.2 Synthesis of LaFeO₃ nanostructure and rGO/LaFeO₃ nanocomposites

LaFeO$_3$ and rGO/LaFeO$_3$ were prepared using hydrothermal process with Pluronic F127 ($C_5H_{10}O_2$) as structure direct agent, La(NO$_3$)$_3$·6H$_2$O and Fe(NO$_3$)$_3$·9H$_2$O as preliminary materials. LaFeO$_3$ microspheres were synthesized as reported in our previous publication [25]. Herein, we discuss the synthesis of LaFeO$_3$ nanostructures incorporated on rGO sheet. In brief, 0.05 g GO was added to 50 ml of milli-Q distilled water and the mixture was sonicated until the GO was completely dispersed in the aqueous solution. Simultaneously, an equi-molar ratio of the starting materials and surfactant (1:1) were dissolved in 50 ml milli-Q distilled water. Both the solution was added dropwise under magnetic stirring continuously for 60 min. After ultrasonication for 30 min, a stable dispersion was obtained and transferred into a 110 ml Teflon-lined stainless steel autoclave and treated under 180 °C for 12 h. The obtained precipitate was washed with absolute alcohol and milli-Q-distilled water several times to remove the unreacted ions and organic impurities followed by drying at 90 °C. The obtained powder was then characterized using different techniques.

2.3 Material characterization and property measurements

Surface morphology and particle size were obtained using SEM (JEOL JSM-6380LV) and HRTEM, (Philips FEI Tecnai 20ST, 200 kV) operated with an acceleration voltage of 200 kV by placing the powder on a copper grid. Crystalline phase of the synthesized samples was characterized by Panalytical X'Pert Pro diffractometer with a conventional X-ray tube (Cu Kα radiation, $\lambda = 1.54$ Å) and Raman analysis (Lab RAM HR 800) with a 514 nm Ar-ion laser (10 mW).

Chemical compositions were confirmed by XPS measurements performed on ESCA+Omicron UK XPS system with a Mg Kα source and a photon energy of 1486.6 eV. All the binding energies were referenced to the C 1s peak at 284.6 eV of the surface adventitious carbon. Surface area analysis was performed using N$_2$ adsorption–desorption analysis taken on an ASAP 2020/Tristar 3000.

2.4 Fabrication and measurement of ozone gas sensor

Details of the gas sensor measurement setup are shown in Fig. 2. Gas sensing properties were tested in a steel-made chamber. A mixture of target gas compressed dry air was flowed at atmospheric pressure at an operating temperature of 100 to 250 °C for optimizing. Two different nanocomposite powders (10 mg) were dispersed in 1 ml of isopropyl alcohol by an ultrasonic for 45 min, and the suspension was dropped onto a Si/SiO$_2$ substrate containing 100 nm thick Pt electrodes separated by a distance of 50 µm.

The substrates were heated to 100 °C for 15 min, followed by calcination at 300 °C for 30 min in an electric furnace in air, to stabilize the sample before gas sensing measurements as shown in Fig. 2. Gas-sensing tests were conducted by exposing the gas sensor device to the analyte gas [ozone gas (UV lamp: UVP, model P/N 90-0004-01)] diluted with dry air in a closed chamber for 5 min. For sensor recovery, dry air was supplied to the chamber for 30 min, using a Keithley 6514 source meter, a signal of the resulting gas sensing device was checked by monitoring the resistance value measured at a voltage of 1 V. The sensing response (S), defined as $S = R_{air}/R_{gas}$, is the electric resistance of the sensor exposed to the resistance in the air (R_{air}) and to the target oxidizing gas (R_{gas}). The response time of the sensor was defined as the time required for a change in the electrical

Fig. 2 Photograph of ozone gas measurement setup and sensing films
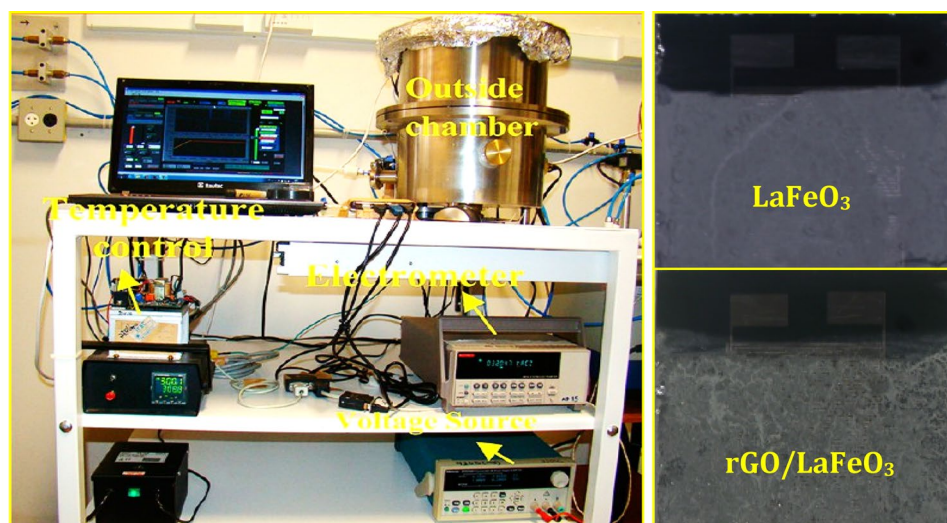
resistance to reach 90% of the initial value when exposed to ozone gas. During the measurements the humidity was under controlled conditions within the range 60% RH.

3 Results and discussion

3.1 Surface morphology and particle size analysis

Surface morphology analysis of prepared GO, rGO, LaFeO$_3$ and rGO/LaFeO$_3$ samples were investigated using scanning electron microscopy (SEM). As can be seen in Fig. 3a, the prepared GO showed wrinkled and folded sheet like structures [26]. Successively, in the wet chemical reaction, these folded sheets of GO were well reduced to two-dimensional (2D) layer-like structure of rGO sheets with curled structures as observed in Fig. 3b. Similar kind of morphology has been observed in previous reports, suggesting the successful formation of rGO [27, 28].

Figure 3c, d indicate that the microsphere with average size ~ 1.5 μm consist of LaFeO$_3$ nanoparticles. The numerous randomly distributed interconnecting nanoparticles were assembled together to form microspheres. In the growth process of microsphere LaFeO$_3$ nanostructure materials, metal ions easily get absorbed on the surfactant ions because of strong interaction between activated oxygen in the surfactant molecular chains and the metal ions. Besides, the LaFeO$_3$ microspheres were uniform in size which can be attributed to dislocations and lattice defects under synthesis condition [29]. 2D graphene sheets are well decorated by a large quantity of LaFeO$_3$ nanostructures, and the outline of both the rGO and the LaFeO$_3$ nanostructures can be clearly observed in Fig. 3e. A detail view of the individual rGO/LaFeO$_3$ microsphere with average size ~ 1 μm is shown in Fig. 3f, which clearly demonstrates that the LaFeO$_3$ nanoparticles were evenly dispersed and incorporated in the rGO sheet. The results indicate that the strong van der Waals interaction among the layers of rGO were overcome, leading to the generation of dispersed LaFeO$_3$ surface via chemisorption [30].

Fig. 3 SEM image of **a** GO, **b** rGO, **c**, **e** low magnification, and **d**, **f** high magnification of LaFeO$_3$ and rGO/LaFeO$_3$ composites
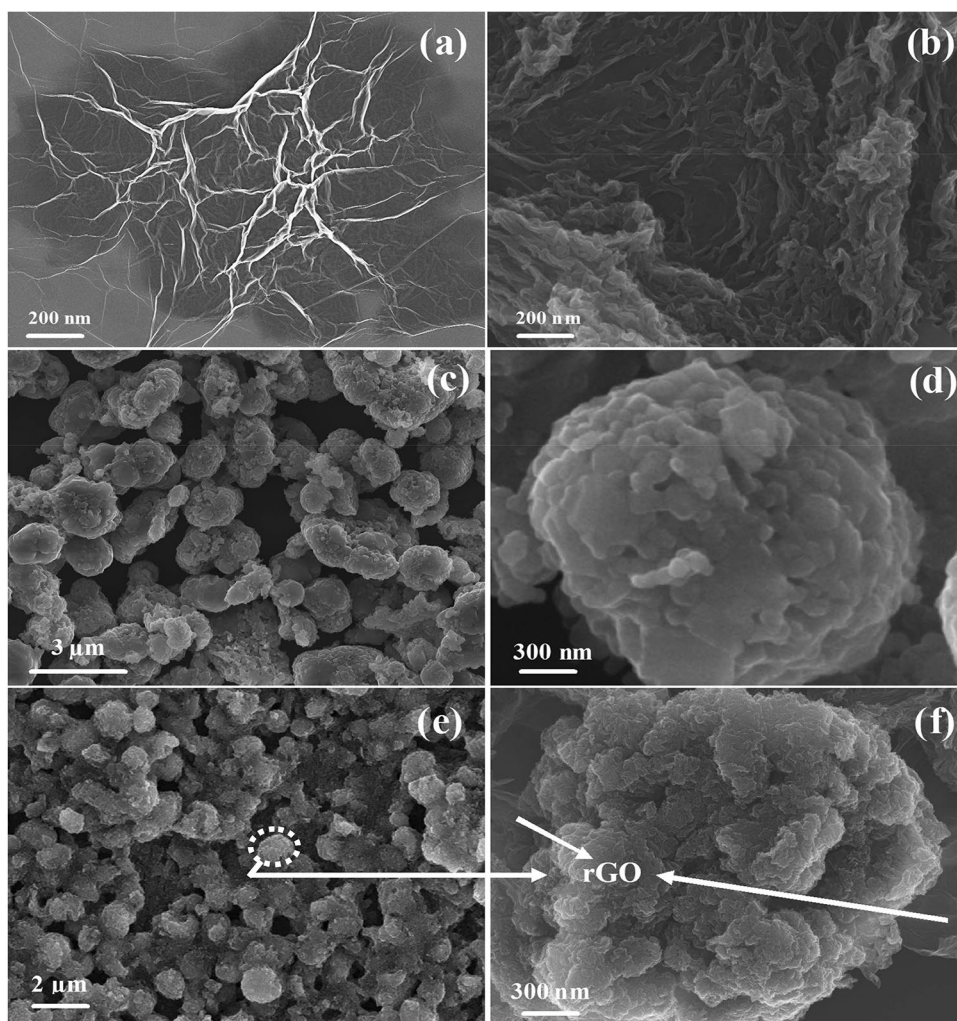
Further investigation in the particle size and crystallographic nature of prepared samples were confirmed by TEM and HRTEM analysis. In the TEM image of LaFeO$_3$ microspheres, it could be clearly noticed that the well-defined microspheres exhibited excellent dispensability with diameter ~ 1.5 µm as confirmed from Fig. 4a. Close observation of LaFeO$_3$ microsphere revealed that they consist of large amount of nanoparticles with average size ~ 90 nm. Most importantly sufficient void spaces in and between the microspheres can be clearly observed in Fig. 4b. HRTEM image represents that the tip of individual LaFeO$_3$ nanoparticles elucidated clear lattice fringes with spacings of 0.281 nm, consistent with the interplanar distances of (121) growth direction as evidenced in Fig. 4c. The SAED pattern (inset Fig. 4c) revealed that the circular rings correspond to diffraction from (121), (202) and (220) reflection planes of the orthorhombic phase, which corresponds to the perovskite LaFeO$_3$ structure respectively. Figure 4d display the rGO/LaFeO$_3$ nanocomposite consistently incorporated on rGO sheets with average size ~ 1 µm, which has good agreement with the SEM observations. The incorporation of LaFeO$_3$ nanostructures in rGO sheets can effectively prevent the microspheres from aggregation, while the rGO sheets can easily form a network with good conductivity. It was reported that numerous wrinkles and folds are beneficial for the rGO sheets to tune the reaction barrier, between the LaFeO$_3$ nanoparticles and rGO sheets. Close observation of rGO/LaFeO$_3$ nanocomposites is shown in Fig. 4e, in which the microsphere constituting

nanoparticles with average size ~ 50 nm, has been uniformly incorporated on the surface of the rGO sheets.

A high resolution TEM image of rGO/LaFeO$_3$ nanocomposites in Fig. 4f, revealed the clear lattice fringes separated by 0.281 and 0.34 nm, which matched well with the (121) and (002) crystal planes of the LaFeO$_3$ orthorhombic structure and rGO sheet respectively. At the top right corner of Fig. 4f (inset), the SAED pattern of the rGO/LaFeO$_3$ nanocomposites can be indexed to the orthorhombic structure of LaFeO$_3$ and major diffraction spots corresponds to (121), (006), and (101) planes. No diffraction spots were attributed to the impurity phases. Thus, by correlating the outcome from TEM and HRTEM images, it can be concluded that the observed results are in good agreement with morphology analysis.

3.2 Structural analysis

Crystal phase and purity of the prepared samples were investigated by XRD analysis as shown in Fig. 5a. It is well known that the GO exhibits a layered structure with an interlayer spacing of 0.81 nm, corresponding to the diffraction peak (002) at 10.24°, revealing the introduction of oxygen functional groups on the expandable graphite sheets [31]. Herein, rGO pattern at $2\theta = 24.95°$ could be indexed to the diffraction peak (002) corresponding to an interlayer distance of 0.34 nm, revealing the removal of oxygen-containing functional groups of GO [31]. The well-defined peaks in the LaFeO$_3$ and rGO/LaFeO$_3$ nanocomposite samples indicate the formation of perovskite phase with orthorhombic

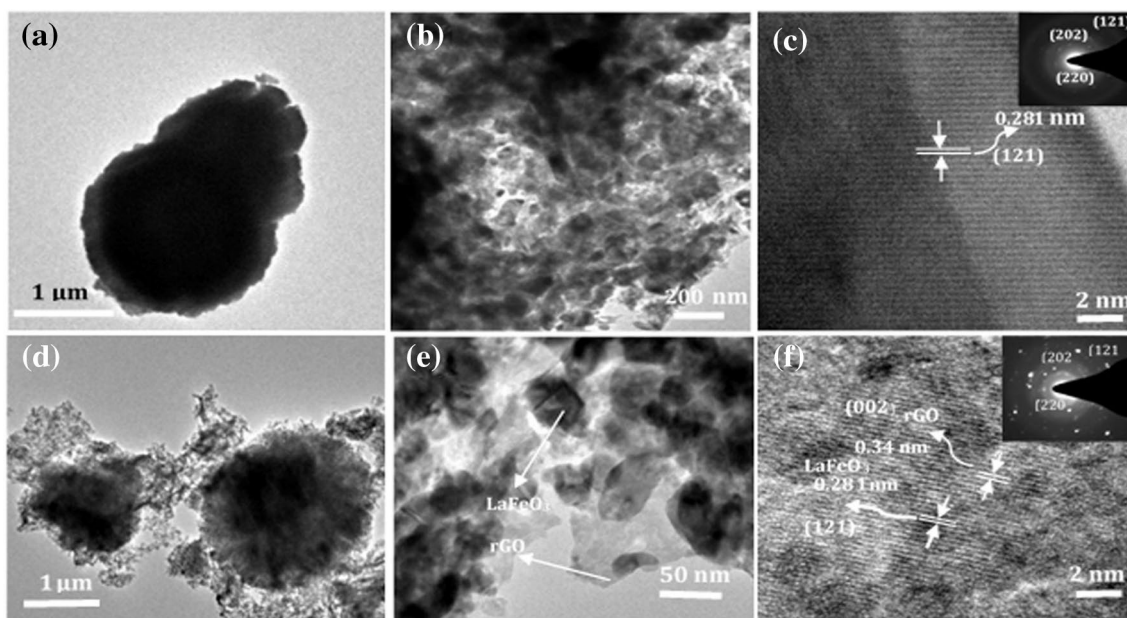**Fig. 4** **a**, **d** Low magnification, **b**, **e** high magnification TEM images, and **c**, **f** HRTEM image of LaFeO$_3$ nanostructures and rGO/LaFeO$_3$ nanocomposites; (inset) corresponding lattice SAED pattern
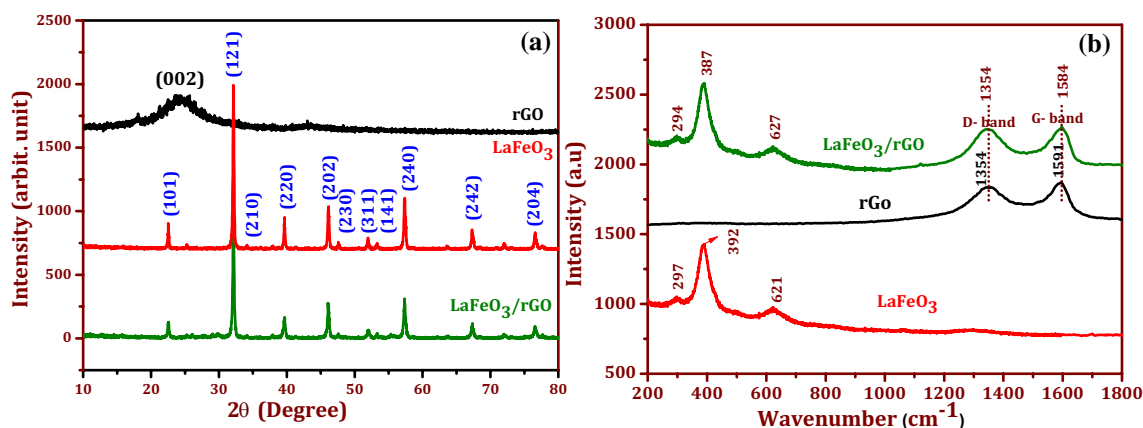
Fig. 5 **a** XRD pattern and **b** Raman spectrum of rGO, LaFeO$_3$ nanostructures and rGO/LaFeO$_3$ nanocomposites

structure, which belongs to the *pbnm* space group with lattice parameter $a = 5.567$–5.569 Å, $b = 7.839$–7.841 Å, and $c = 5.576$–5.578 Å (within a maximum experimental error of ± 0.0002), well matched with the standard values (JCPDS# 37-1493) [32].

No other crystalline phases and other impurity phases were detected in the XRD pattern, indicating that the prepared samples with high purity could be obtained under synthetic conditions. However, there are no rGO related diffraction peaks in rGO/LaFeO$_3$ nanocomposites because of the low loading of GO and the disordered stacking of the rGO sheets in the synthesis condition. The average crystallite size was calculated using Debye–Scherrer formula [33] and found to be ~ 87 nm for LaFeO$_3$ nanostructure and ~ 53 nm for rGO/LaFeO$_3$ nanocomposites respectively, these values are in good agreement with the results obtained from the morphological analysis.

Figure 5b represents the Raman spectra of rGO, LaFeO$_3$ nanostructure and rGO/LaFeO$_3$ nanocomposites. The Raman spectrum of GO usually reveals two main bands D and G at 1354 and 1591 cm^{-1} respectively. The D band is attributed to the defect-induced breathing mode of sp^3 hybridized carbon and structural imperfections in the graphite layer, whereas the G band results from E$_{2g}$ mode consisting of sp^2 hybridized C–C bonds in a 2D hexagonal lattice [34]. Further, Raman modes of synthesized LaFeO$_3$ nanostructures at 297 cm^{-1} due to A$_g$ assigned modes of two-photon scattering can be associated with La–O and 392 cm^{-1} peak represents the B$_{3g}$ mode due to in-plane vibration of Fe–O [35]. In addition, the 621 cm^{-1} peak can be related to two-photon scattering of "O^{2-}" and the 387 and 627 cm^{-1} peaks correspond to rGO/LaFeO$_3$ nanocomposites. The red shift of the wavenumber positions of bending and stretching modes of LaFeO$_3$ nanostructures grown over the rGO sheet when compared to their pure LaFeO$_3$ nanostructures may be due to the incorporation of LaFeO$_3$ nanostructures with the surface

of the rGO sheet. In addition, for the Raman bands of rGO sheet incorporated with LaFeO$_3$, the D and G bands have also been observed at 1354 and 1583 cm^{-1} respectively. This indicates that the LaFeO$_3$ nanostructure have been grown over the rGO sheet, which could not be confirmed by analyzing the XRD data. The values of I_D/I_G for rGO/LaFeO$_3$ and rGO were calculated as 0.89 and 1.02, respectively. The reduced value of I_D/I_G in case of rGO/LaFeO$_3$ composite indicates that the number of sp^2 bonded carbon atoms has been increased during the in situ synthesis of rGO/LaFeO$_3$ nanocomposites. It means that the damaged sp^2 network was repaired in case of in situ synthesis condition. These results are in good agreement with the results obtained from XRD analysis.

3.3 Chemical composition analysis

Chemical state and composition of prepared samples GO, LaFeO$_3$ nanostructures and rGO/LaFeO$_3$ nanocomposites were obtained using XPS analysis. The binding energies carried out were corrected for specimen charging by referencing the C 1s line to 284.6 eV.

Figure 6a represents the typical XPS survey spectrum of the GO, LaFeO$_3$ nanostructures and rGO/LaFeO$_3$ nanocomposites which reveals the presence of La (3d), Fe (2p), O (1s), and C (1s). The La 3d and Fe 2p core-level spectra reveal that for the LaFeO$_3$ nanostructures and rGO/LaFeO$_3$ nanocomposites, lanthanum and iron atoms are in the formal chemical valence state +3 [36]. Two strong La peaks 3d$_{5/2}$ were observed at 833.7–834.5 eV and peak for 3d$_{3/2}$ at 850.9–851.5 eV, which corresponds to spin–orbit splitting of La^{3+} ions in oxide form. The binding energies of Fe 2p$_{3/2}$ and Fe 2p$_{1/2}$ were observed at 709.2–708.5 eV and 723.7–734.5 eV which correspond to Fe^{3+} ions in oxide form [37]. The presence of C element in GO and rGO/LaFeO$_3$ nanocomposites samples were confirmed from the
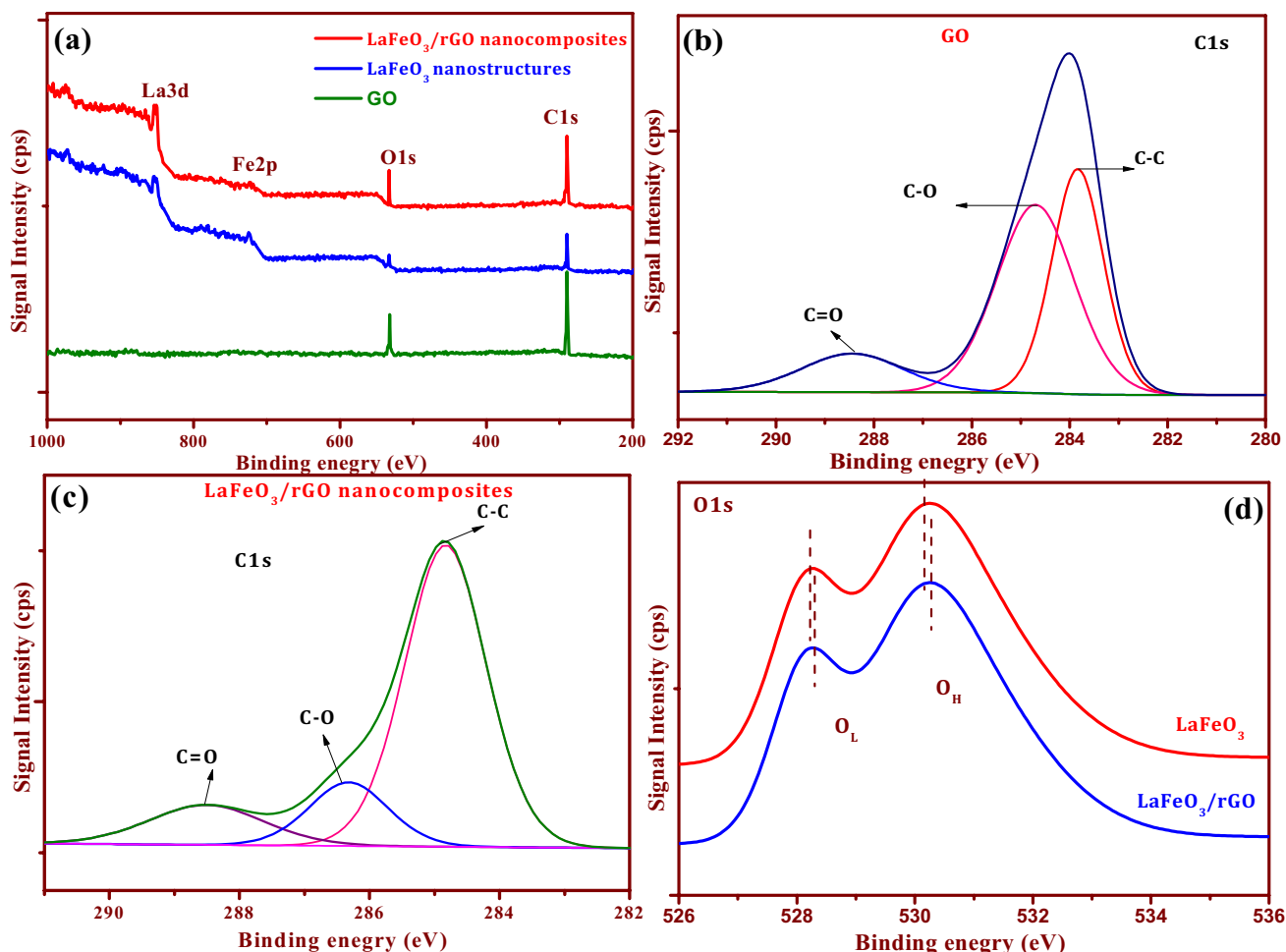
Fig. 6 **a** XPS survey spectra, **b** C 1s line after offset of GO, **c** C 1s line after offset of rGO/LaFeO$_3$ nanocomposites and **d** local fine scanning of O 1s for LaFeO$_3$ nanostructure and rGO/LaFeO$_3$ nanocomposites

XPS spectrum represented in Fig. 6b, c. It was observed that the C 1s spectra of GO and rGO/LaFeO$_3$ nanocomposite samples could be deconvoluted into three Gaussian peaks with binding energies at 284.2, 286.9 and 288.9 eV associated with [C–C, C–O] and C=O, respectively. Compared with the peak intensity of C–O and C=O in GO sample, the rGO/LaFeO$_3$ nanocomposite samples peak intensities of C–O and C=O decrease obviously, indicating that GO has been restored to rGO successfully with some amount of residual oxygenic groups as shown in Fig. 6b. The GO spectrum dominated by a C–C band with a binding energy at 284.2 eV could be due to sp^2 carbon, suggesting the restoration of the graphene network in the synthesized hybrid composite. The binding energy at 528.2 and 527.1 eV of the OL XPS signal can be attributed to the contribution of La–O and Fe–O in the LaFeO$_3$ crystal lattice as shown in Fig. 6d. The OH XPS signal at 530.5 and 529.2 eV can be assigned to the oxygen of the hydroxide ions, and the peak shift observed can be attributed to the residual oxygen-containing groups

in rGO. The oxygen-containing functional groups of continuous electronic conductive networks, could impact fast charge carrier transport which significantly improve the sensing behaviour and maintain the reliability of the rGO/LaFeO$_3$ nanocomposites.

3.4 Surface area analysis

The specific surface area and pore volume of LaFeO$_3$ nanostructure and rGO/LaFeO$_3$ nanocomposites were confirmed by nitrogen physisorption measurements. Both samples reveal the typical absorption/desorption isotherm of type IV with an H3 hysteresis loop at a relative high pressure between $0.8 < P/P_0 < 1.0$, characteristic for mesoporous with different pore sizes as shown in Fig. 7a, b.

The specific surface area of LaFeO$_3$ nanostructure was 107 m^2 g^{-1} with a pore volume of 0.14 cm^3 g^{-1} while the specific surface area of rGO/LaFeO$_3$ nanocomposites increases to 242 m^2 g^{-1} with a pore volume of 0.27 cm^3 g^{-1},
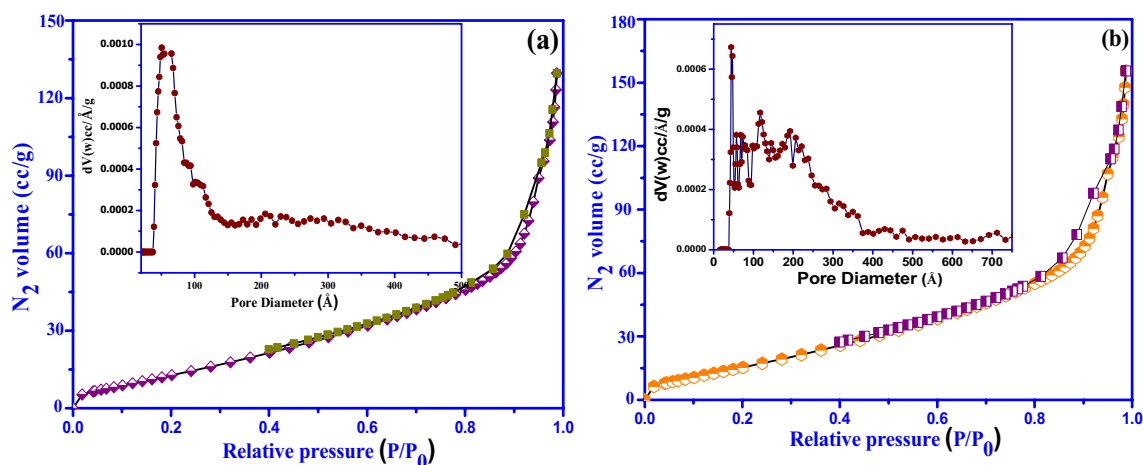
Fig. 7 Nitrogen adsorption–desorption isotherms and the corresponding pore size distribution of **a** LaFeO$_3$ nanostructures and **b** rGO/LaFeO$_3$ nanocomposites

due to the incorporation of rGO. Furthermore, the pore volume distribution curve as a function of the pore size distribution of LaFeO$_3$ nanostructure and rGO–LaFeO$_3$ nanocomposites were calculated using the Barrett–Joyner–Halenda (BJH) model presented in the inset of Fig. 7a, b. LaFeO$_3$ samples have uniform pore size distribution with an average pore size of ∼ 2–5 nm and for rGO–LaFeO$_3$ nanocomposites, two different peaks can be clearly noticed. The first high intensity peak may correspond to the small nanospheres constituting the microspheres. On the other hand, the second-high intensity peak correspond to the composite of rGO sheet. These results suggest that the greatly increased surface area and pore volume of rGO–LaFeO$_3$ nanocomposites may be due to the activation hybrid effect of LaFeO$_3$ surface on rGO sheet [38]. This paves way for fascinating adsorbing ability of analyte during gas sensing, which would be

valuable to achieve an improved toxic gas selectivity and sensitivity performance, at ppb level detection limit.

3.5 Ozone gas sensor performance of LaFeO$_3$ and rGO/LaFeO$_3$ nanocomposites

Sensitivity, selectivity, stability, operating temperature and gas concentration are the important parameters for toxic gas analysis. However, selectivity plays a major role in toxic gas sensing measurement. In the present work, ozone (O$_3$), NH$_3$, CO and NO$_2$ sensing were carried out for different concentrations at 100 °C, and the response for each gas were recorded as shown in Fig. 8a. The sensing device demonstrate a comparatively lower response for NO$_2$ (2 ppm), NH$_3$ (5 ppm) and CO (10 ppm). However, high response at low concentration (80 ppb) to O$_3$ can be due to the reaction with
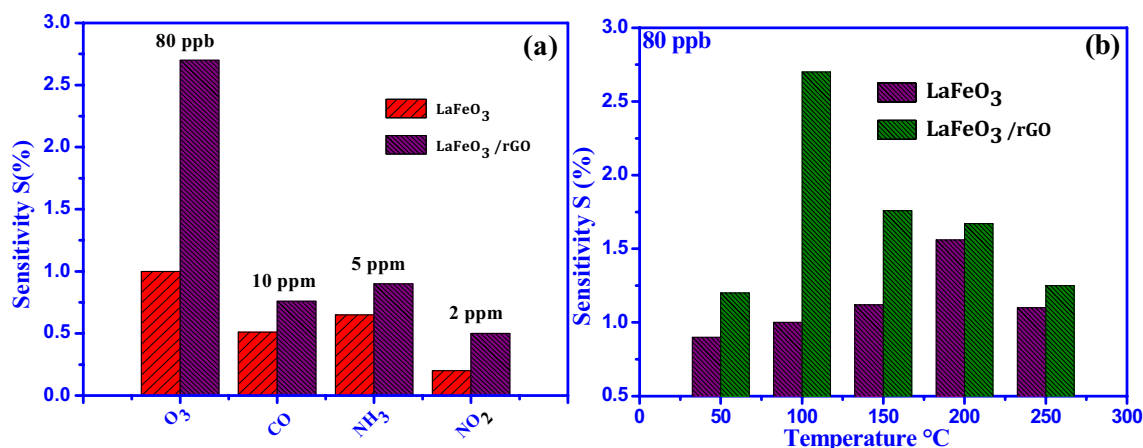

Fig. 8 **a** Different target gases sensing response and **b** the response for O$_3$ for 80 ppb by the LaFeO$_3$ nanostructure and rGO/LaFeO$_3$ nanocomposites working at different temperatures

the adsorbed oxygen ions on the rGO/LaFeO$_3$ nanocomposite sensing device surface and catalytic activity with O$_3$ molecules. Moreover, electron receiving capacity of O$_3$ was better than other toxic gases because of the presence of lone-pair holes. The film showed a comparatively lower response for O$_3$, NH$_3$, ammonia, CO, and N$_2$. The reason for the high response to O$_3$ can be due to the change in resistance for oxidizing gases, reaction with the adsorbed oxygen ions on the sensor surface, optimum porosity of the film, crystallite size, and catalytic activity of LaFeO$_3$ or rGO/LaFeO$_3$ with O$_3$ molecules. Moreover, electron acceptor ability of Ozone is higher than that of other vapours because of the presence of lone pair of holes [39]. The fabricated gas sensor is practically insensitive to the other common interference gases, showing more selectivity toward O$_3$ gas.

Figure 8b represents the ozone sensitivity performance of LaFeO$_3$ nanostructure and rGO/LaFeO$_3$ nanocomposites exposed to 80 ppb for reactive oxidizing gas molecule (ozone) at various operating temperature between 50 and 250 °C with intervals of 50 °C having an experimental error of $\pm 0.01\%$. The response of LaFeO$_3$ nanostructure sensitivity was initially low, which then increased and reached its maximum at 200 °C, followed with a decrease with further increase in operating temperature to 250 °C because of the slow kinetic energy of gas molecules at low temperature

and their enhanced desorption at high temperature. The response of rGO/LaFeO$_3$ nanocomposites to 80 ppb of ozone gas reached its maximum at 100 °C. Also, when the operating temperature was increased upto 250 °C, the gas sensing response decreased, because the LaFeO$_3$ nanostructures incorporating the rGO requires enough thermal energy to be activated at low operating temperature and the chemical activation requires sufficient thermal energy to cause the sensitivity, as well these could effect of the rGO behaviour for thermally excited electrons [40].

The difference in the optimum operating temperature with high sensitivity of the LaFeO$_3$ nanostructure (200 °C) and rGO/LaFeO$_3$ nanocomposites (100 °C) ozone gas sensors could be originated from their different oxygen absorption capabilities. For the rGO/LaFeO$_3$ nanocomposites samples, the response was noticeably excellent with respect to LaFeO$_3$ nanostructure at all operating temperature because of the strong synergistic effect between rGO and LaFeO$_3$, also large surface area maximizes the exposure to analyte. Consequently, carrier's transport can also move rapidly with little resistance through the continuous and interconnected graphene networks and enhance sensitivity and selectivity.

Figure 9a, c shows the dynamic response–recovery curves of the LaFeO$_3$ nanostructure and rGO/LaFeO$_3$ nanocomposites exposed to ozone gas for continuous three cycles and
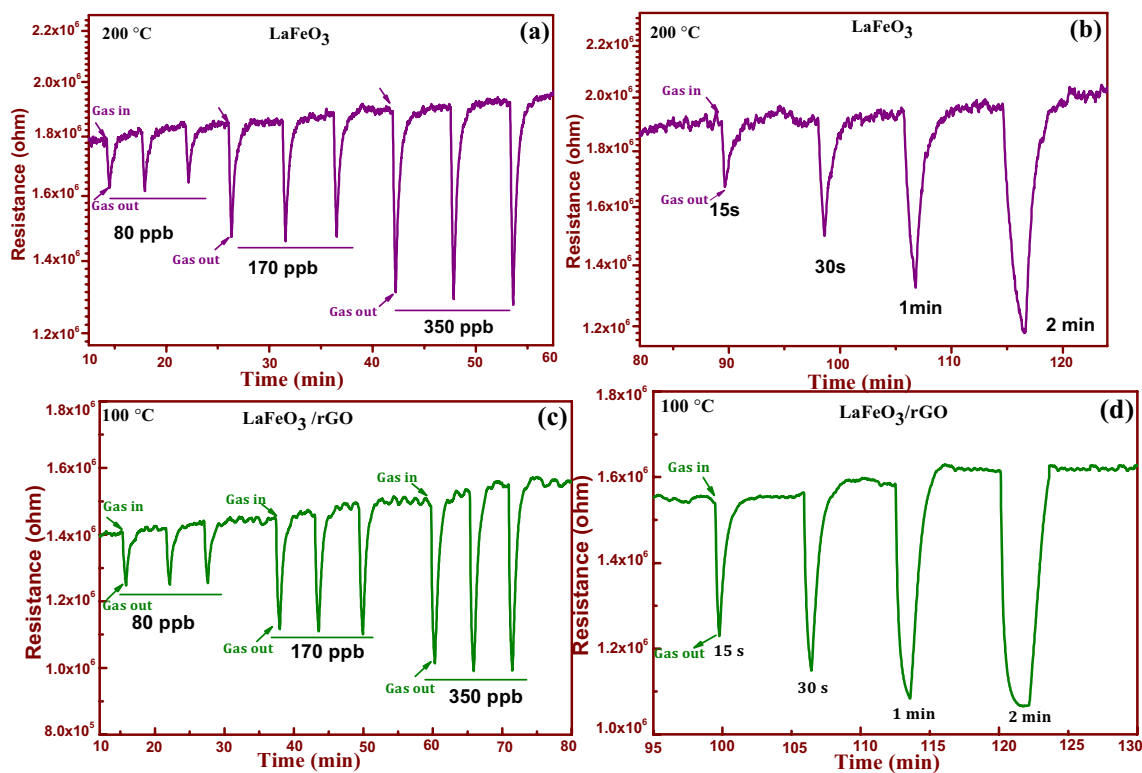

Fig. 9 **a**, **c** Transient sensing response of different concentrations (80, 170, 350 ppb) and **b**, **d** various time (15 s, 30 s, 60 s, 120 s) of ozone (O$_3$) gas of LaFeO$_3$ (200° C) and rGO/LaFeO$_3$ (100° C)

different concentrations (80, 170 and 350 ppb) were studied. The results of all three tested gas concentration reveals good stability behaviour due to the operating temperature with regard to the mechanics and kinetics of gas adsorption on the surface of sensing materials. At different gas exposure time (15 and 30 s, 1 and 2 min) as shown in Fig. 9b, d, the fabricated sensing materials has an excellent stability.

Figure 10a reveals the gas response of $LaFeO_3$ nanostructure and $rGO/LaFeO_3$ nanocomposites as a function of various concentration of ozone gas at 100 °C. The results indicate that the sensing response increased with the increase in ozone gas concentration (80, 170, 350 ppb) and the sensitivity were found to be 0.9, 1.1 and 1.5 for $LaFeO_3$ nanostructure and 2.6, 3.0 and 3.3 for $rGO/LaFeO_3$ nanocomposites with an experimental error of ±0.01%, respectively. For the prepared nanostructure materials, sensing response increased as the concentration increased, which can be attributed to the number of oxygen-adsorption sites. This shows clearly that the $rGO/LaFeO_3$ nanocomposite sensors exhibit an enhanced and superior gas sensing response for 80 ppb concentration compared with $LaFeO_3$ nanostructures. The reason mainly attributes to the incorporation of rGO sheet with $LaFeO_3$ nanostructures leading to more active sites and oxygen functional groups for the adsorption of gas molecules [41].

The long-term sensing stability of $LaFeO_3$ nanostructure and $rGO/LaFeO_3$ nanocomposites were evaluated by exposing the sensor to 350 ppb of O_3 at 100 °C over a period of 10 weeks at intervals of 1 week as shown in Fig. 10b. The gas sensor response varied slightly with increase in the resistance baseline and subsequent decrease in the sensor response to O_3 at low concentration over long time stability. It can be evidenced that the $rGO/LaFeO_3$ nanocomposites show excellent sensitivity toward ozone gas when compared

to $LaFeO_3$ nanostructure at 10 weeks time. This can be attributed to the unique morphology, efficient adsorption and desorption of the analyte gas, incorporation of rGO and also particle size.

The temperature-dependent response and recovery time of $LaFeO_3$ nanostructure and $rGO/LaFeO_3$ nanocomposites are shown in Fig. 11a, b. At lower temperature of 100 °C, the response (31 and 20 s) and recovery time (39 and 31 s) for $LaFeO_3$ nanostructure and $rGO/LaFeO_3$ nanocomposites, demonstrate the quick response-recovery characteristics of the sensor to 80 ppb for $rGO/LaFeO_3$ nanocomposites. Because the sensing operating temperature regulates the activation energies of adsorption/desorption and thereby the kinetics of the surface chemisorption reactions. Fast mass transfer of ozone molecules from the interaction region improves the rate for charge carriers to traverse the barriers induced by molecular recognition in the $rGO/LaFeO_3$ nanocomposites.

In addition, for 250 °C the response and recovery time was very high and shows an increasing trend with increase in operating temperature. On other side, for low temperature, time required for the complete reaction of the oxygen species and ozone molecules lead to short response time. At higher temperature, more ozone molecules interact with the oxygen ions and increase the response and recovery time. The recovery time of $rGO/LaFeO_3$ nanocomposites materials were lesser than other reported p-type and *n*-type sensor materials such as CuO, $SrTiO_3$, In_2O_3 and SnO_2 etc. [34, 42, 43]. From the above results, we confirm that the response of the two different sensing materials—$LaFeO_3$ nanostructure and $rGO/LaFeO_3$ nanocomposites towards ozone gas strongly depends on the operating temperature, surface area, particle size, incorporation of rGO as well as the concentration of test gas. The results clearly demonstrate that there is
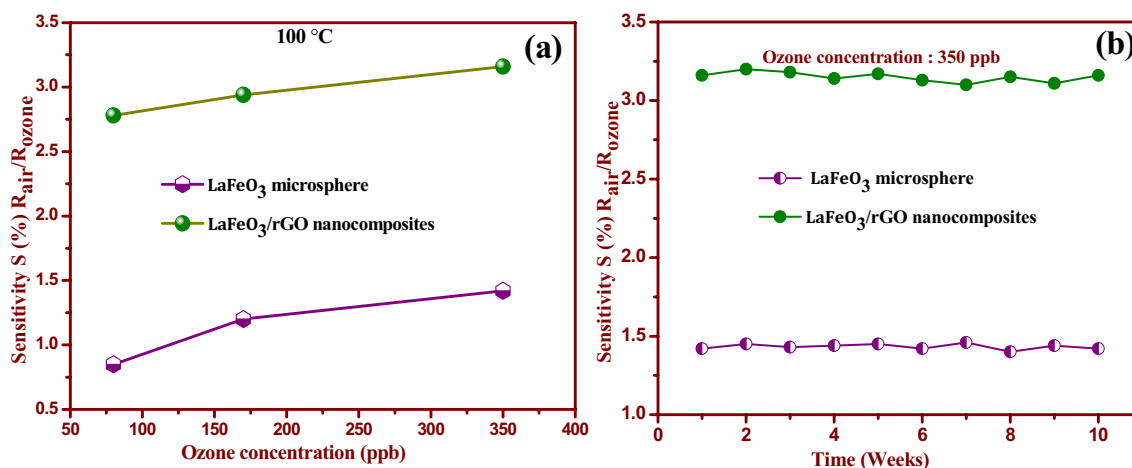

Fig. 10 **a** Sensing response as a function of ozone concentration (80 ppb, 170 ppb and 350 ppb) and **b** long-term stability of $LaFeO_3$ nanostructure and $rGO/LaFeO_3$ nanocomposites
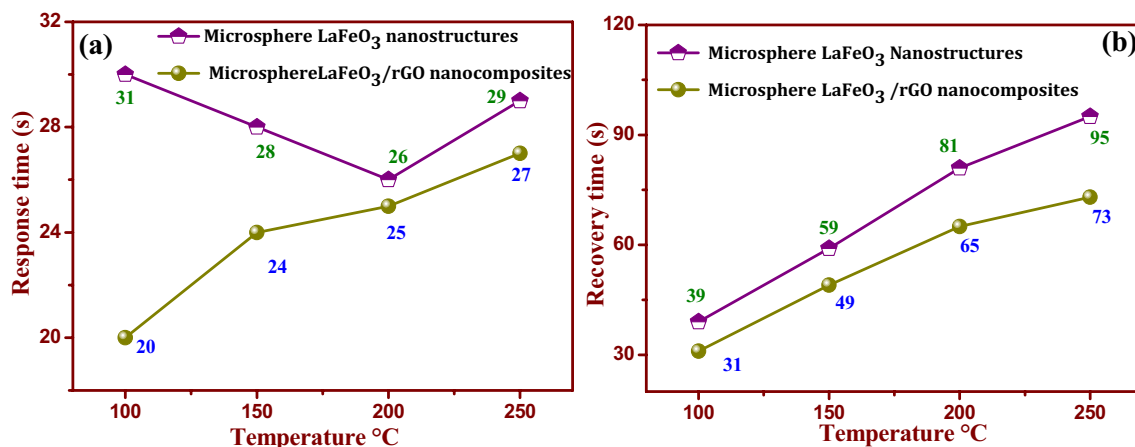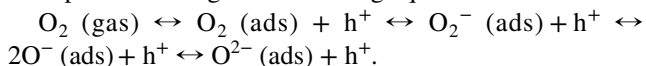
Fig. 11 **a** Response time (s) and **b** recovery time (s) of the statistical reports of microspheres LaFeO$_3$ nanostructures and microsphere rGO/LaFeO$_3$ nanocomposites

great advantage of employing the present fabrication route which is cost-effective to prepare rGO/LaFeO$_3$ nanocomposites for real-time monitoring of ozone gas sensor for 80 ppb at 100 °C.

3.6 Sensing mechanism of LaFeO$_3$ nanostructure and rGO/LaFeO$_3$ nanocomposites

It was demonstrated that the oxidizing gas (O$_3$) can be chemisorbed on the LaFeO$_3$ nanostructure and rGO/LaFeO$_3$ nanocomposites because LaFeO$_3$ and rGO performs as p-type i.e. majority carrier are holes. The acceptor level lies near the valence band, and at operating temperature all the acceptor levels are ionized (filled) leaving holes in the valence band. The incorporation of rGO sheets to LaFeO$_3$ nanostructure provides outstanding physicochemical properties, high surface-to-volume ratio and unique electrical conductivity. As LaFeO$_3$ nanostructure and rGO/LaFeO$_3$ nanocomposites surface were exposed to air, the adsorption of atmospheric oxygen species on the sensor surface forms ionic species O$_2^-$, O$^-$, and O^{2-} ions by trapping electrons from the conduction band. The adsorption of oxygen with positive charges can generate holes, resulting in the formation of a hole accumulation-layer (HAL). The reaction kinetics can be explained through the following equation

O$_2$ (gas) $\leftrightarrow$ O$_2$ (ads) + h$^+$ $\leftrightarrow$ O$_2^-$ (ads) + h$^+$ $\leftrightarrow$ 2O$^-$ (ads) + h$^+$ $\leftrightarrow$ O^{2-} (ads) + h$^+$.

When the oxidation gas ozone (O$_3$) was introduced at the surface of LaFeO$_3$ nanostructure and rGO/LaFeO$_3$ nanocomposites, the ozone molecules adsorb on the sensing materials surface acting as acceptors. This surface trapping of lone-pair electrons results in the formation of free holes and an increase in hole concentration near the interface forming the hole accumulation-layer at the surface of LaFeO$_3$ nanostructure and rGO/LaFeO$_3$ nanocomposites which decrease

the resistance. The following equation represents the process taking place on the surface of rGO/LaFeO$_3$ sample for oxidation gases.

LaFeO$_3$ (or) LaFeO$_3$–rGO + O$_3$ (gas) $\leftrightarrow$ LaFeO$_3^+$ − O$_3^-$ $\leftrightarrow$ LaFeO$_3^-$ O$_3^-$ (ads) + h.
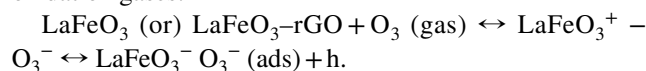
We can observe that the rGO/LaFeO$_3$ nanocomposites have small grain size (D_G) compared to LaFeO$_3$ nanostructures, and thus better gas-sensing sensitivity. rGO/LaFeO$_3$ nanocomposites with tiny nanoparticle size ~ 50 nm presents a higher surface to volume ratio, according to the 'small size effect', when D_G (particle size) $< D_N$ (width of the space-charge layer), the space-charge layer region dominates the whole particle, so a few charges acquired from the surface reaction will cause large changes in conductivity of the whole structure as shown in Fig. 12. Gas sensing response increases with decrease in grain size (D_G), increased neck diameter (D_N) and grain to grain contact [44].

Here, LaFeO$_3$ nanostructure have a larger grain size, face to face grain contact and small neck diameter (D_N) when compared to rGO/LaFeO$_3$ nanocomposites. This provides highly exposed surfaces and more pathways for electron exchange during gas diffusion/molecule capture and surface reaction. LaFeO$_3$ were incorporated with rGO sheet as a conducting channel surface because of higher accessibility, more effective transit carriers and exhibit high sensitivity towards ozone gas at low temperature of 100 °C.

4 Conclusions

In summary, we obtained LaFeO$_3$ nanostructure and rGO/LaFeO$_3$ nanocomposites with average size ~ 90 nm and ~ 50 nm of good surface area 107 and 242 m^2 g^{-1}. Surface morphology and crystal structure confirmed that the prepared materials exhibit orthorhombic perovskite structure. XPS

Fig. 12 Schematic diagram of surface processes associated with the reaction at ambient oxygen (left) and ozone gas (oxidation gas) (right) and (LD Debye length, D_N size of neck, D_G size of particle) for microsphere LaFeO$_3$ nanostructures and microsphere rGO/LaFeO$_3$ nanocomposites
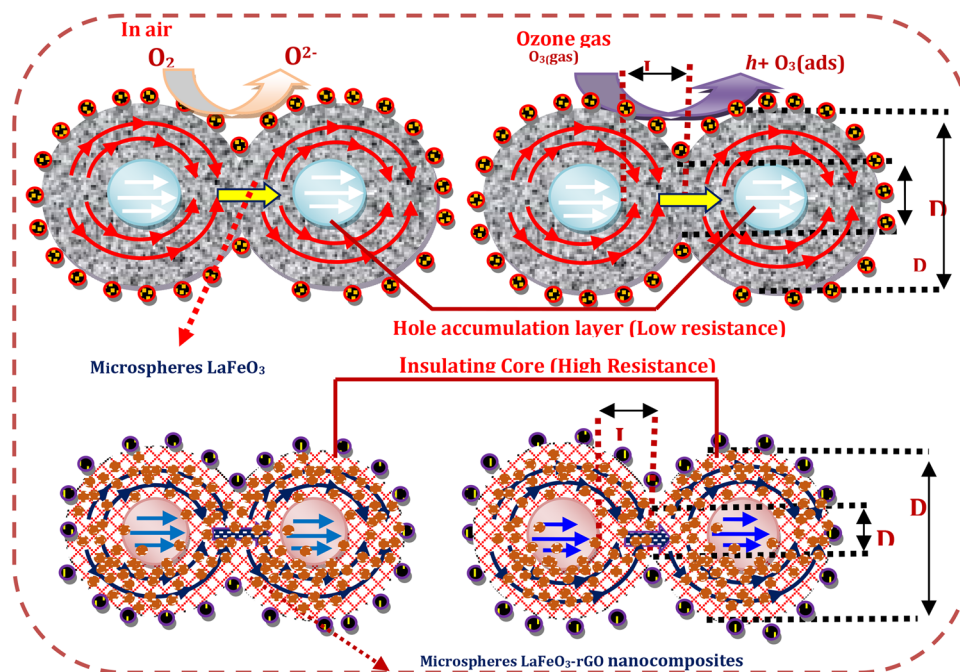
analysis revealed that a large amount of oxygen vacancies appearing on the surface directly contributed to the enhanced sensor response. The gas sensing analysis of rGO/LaFeO$_3$ nanocomposites have exhibited high sensitivity, excellent selectivity, quick response time and long-time stability towards ozone gas concentration of 80 ppb at low-operating temperature 100 °C compared to LaFeO$_3$ nanostructure and also other reported work. We believe that remarkable performance of ozone gas sensor was achieved at ppb detection level of toxic gas for low operating temperature during real time monitoring which can pave way for environmental remediation process.

References

1. C. Pang, G.Y. Lee, T. Kim, S.M. Kim, H.N. Kim, S.H. Ahn, K.Y.A. Suh, Flexible and highly sensitive strain gauge sensor using reversible interlocking of nanofibres. Nat. Mater. **11**(9), 795–801 (2012)
2. J. Zhang, Z. Qin, D. Zeng, C. Xie, Metal oxide semiconductor-based gas sensors: screening, preparation, and integration. Phys. Chem. Chem. Phys. **19**, 6313–6329 (2013)
3. W. Belkacem, A. Labidi, J. Guerin, N. Mliki, K. Aguir, Cobalt nanograins effect on the ozone detection by WO$_3$ sensors. Sens. Actuators B **132**(1), 196–201 (2008)
4. J.H. Kim, J.H. Lee, Highly sensitive and selective gas sensors using p-type oxide semiconductors: overview. Sens. Actuators B **192**, 607–627 (2014)
5. R.M. Valmor, C.Z. Sergio, L.F. Silva, I.P. Pedro, B. Maria, G. Jacques, A. Khalifa, Ozone gas sensor based on nanocrystalline SrTi$_{1-x}$Fe$_x$O$_3$ thin films. Sens. Actuators B **181**, 919–924 (2013)
6. World Health Organization, *Air Quality Guidelines Global Update 2005, WHO Regional Publications, European Series* (World Health Organization, Regional Office for Europe, Copenhagen, 2006)
7. J.X. Zhao, L.X. Zhang, X.Y. Xie, X.H. Li, Y.J. Ma, W.H. Fang, X.F. Shi, G.L. Cui, X.P. Sun, Ti$_3$C$_2$T$_x$ (T = F, OH) MXene nanosheets: conductive 2D catalysts for ambient electro hydrogenation of N$_2$ to NH$_3$. J. Mater. Chem. A **6**, 24031–24035 (2018)
8. S. Yasuda, Y. Li, J. Kim, K. Murakoshi, Selective nitrogen doping in graphene for oxygen reduction reactions. Chem. Commun. **49**, 9627–9629 (2013)
9. F. Schedin, A.K. Geim, S.V. Morozov, E.W. Hill, P. Blake, M.I. Katsnelson, K.S. Novoselov, Detection of individual gas molecules adsorbed on graphene. Nat. Mater. **6**, 652–655 (2007)
10. Z. Zhang, X. Zou, L. Xu, L. Liao, W. Liu, H. Johnny, X. Xiao, C. Jiang, J. Li, Hydrogen gas sensor based on metal oxide nanoparticles decorated graphene transistor. Nanoscale **7**, 10078–10084 (2015)
11. S.R. Aliwell, J.F. Halsall, K.F.E. Pratt, R.L. Jones, R.A. Cox, S.R. Utembe, G.M. Hansford, D.E. Williams, Ozone sensors based on WO$_3$: a model for sensor drift and a measurement correction method. Meas. Sci. Technol. **12**, 684–690 (2001)
12. G. Korotcenkov, B.K. Cho, Ozone measuring: what can limit application of SnO$_2$-based conductometric gas sensors. Sens. Actuators B **161**, 28–44 (2012)
13. X. Gao, T. Zhang, An overview: facet-dependent metal oxide semiconductor gas sensors. Sens. Actuators B **277**, 604–633 (2018)
14. S. Thirumalairajan, K. Girija, V.R. Mastelaro, N. Ponpandian, Surface morphology-dependent room-temperature LaFeO$_3$ nanostructure thin films as selective NO$_2$ gas sensor prepared by radio frequency magnetron sputtering. ACS Appl. Mater. Interfaces **6**, 13917–13927 (2014)
15. A. Mirzaei, J.H. Kim, H.W. Kim, S.S. Kim, Resistive based gas sensors for detection of benzene, toluene and xylene (BTX) gases: a review. J. Mater. Chem. C **6**, 4342–4370 (2018)

16. G.C. Shyamasree, C. Somenath, K.R. Ajoy, K.C. Amit, Graphene-metal oxide nanohybrids for toxic gas sensor: a review. Sens. Actuators B **221**, 1170–1181 (2015)

17. X. Lin, X. Shen, Q. Zheng, J.K. Kim, Fabrication of highly-aligned, graphene papers using ultra large graphene oxide sheets. ACS Nano **6**, 10708–10719 (2012)

18. Z. Song, Z. Wei, B. Wang, Z. Luo, S. Xu, Sensitive RT H_2S gas sensors employing SnO_2 quantum wire/rGO nanocomposites. Chem. Mater. **28**, 1205–1212 (2016)

19. P. Wang, D. Wang, M. Zhang, Y. Zhu, Y. Xu, X. Ma, ZnO nanosheets/graphene oxide nanocomposites for highly effective acetone vapor detection. Sens. Actuators B **230**, 477–484 (2016)

20. M. Epifani, E. Comini, J. Arbiol, Chemical synthesis of In_2O_3 nanocrystals and their application in highly performing ozone-sensing devices. Sens. Actuators B **130**, 483–487 (2008)

21. T. Kei, F. Ryo, H. Shinya, Recent progress in applications of graphene oxide for gas sensing: a review. Anal. Chim. Acta **878**, 43–53 (2015)

22. R.K. Mishra, S.B. Upadhyay, A. Kushwaha, G. Murali, S. Manish, SnO_2 quantum dots decorated on rGO: a superior sensitive, performance for a H_2 and LPG sensor. Nanoscale **7**, 11971–11979 (2015)

23. S. Jinjin, Z. Cheng, L. Gao, Y. Zhang, J. Xu, H. Zhao, Facile synthesis of reduced graphene oxide/hexagonal WO_3 nanosheets composites with enhanced H_2S sensing properties. Sens. Actuators B **230**, 736–745 (2016)

24. W.S. Hummers, Preparation of graphitic oxide. J. Am. Chem. Soc. **80**, 1339 (1958)

25. S. Thirumalairajan, K. Girija, R.M. Valmor, V. Ganesh, N. Ponpandian, Detection of the neurotransmitter dopamine by a glassy carbon electrode modified with perovskite $LaFeO_3$ microspheres made up of nanospheres. RSC Adv. **4**, 25957–25962 (2014)

26. T. Niu, G.L. Liu, Y. Chen, J. Yang, Y. Cao, Y. Liu, Hydrothermal synthesis of graphene–$LaFeO_3$ composite supported with Cu–Co nanocatalyst for higher alcohol synthesis from syngas. J. Appl. Surf. Sci. **364**, 388–399 (2016)

27. Y. Xia, J. Wang, J.L. Xu, X. Li, D. Xie, L. Xiang, S. Komarneni, Confined formation of ultrathin ZnO nanorods/reduced graphene oxide mesoporous nanocomposites for high-performance room-temperature NO_2 sensors. ACS Appl. Mater. Interfaces **8**, 35454–35463 (2016)

28. H. Meng, W. Yang, K. Ding, L. Feng, Y.F. Guan, Cu_2O nanorods modified by rGO for NH_3 sensing at room temperature. J. Mater. Chem. A **3**, 1174–1181 (2015)

29. R.S. Dey, S. Hajra, R.S. Sahu, C.R. Raj, C.M. Panigrahi, A rapid room temperature chemical route for the synthesis of graphene: metal-mediated reduction of graphene oxide. Chem. Commun. **48**, 1787–1789 (2012)

30. X. Ren, H.T. Yang, S. Gen, J. Zhou, T.Z. Yang, X.Q. Zhang, Z.H. Cheng, S.H. Sun, Controlled growth of $LaFeO_3$ nanoparticles on reduced graphene oxide for highly efficient photocatalysis. Nanoscale **8**, 752–756 (2016)

31. Z.J. Fan, W. Kai, J. Yan, T. Wei, L.J. Zhi, J. Feng, Y. Ren, L.P. Song, F. Wei, Facile synthesis of graphene nanosheets *via* Fe reduction of exfoliated graphite oxide. ACS Nano **5**, 191–198 (2011)

32. D. Kumar, R. Jayavel, Facile hydrothermal synthesis and characterization of $LaFeO_3$ nanospheres for visible light photocatalytic applications. J. Mater. Sci. Mater. Electron. **25**, 3953–3961 (2014)

33. K. Girija, S. Thirumalairjan, D. Mangalaraj, Photocatalytic degradation of organic pollutants by shape selective synthesis of β-Ga_2O_3 microspheres constituted by nanospheres for environmental remediation. J. Mater. Chem. A **3**, 2617–2627 (2015)

34. C. Wang, J. Zhu, S. Liang, H. Bi, Q. Han, X. Liu, X. Wang, Reduced graphene oxide decorated with CuO–ZnO hetero-junctions: towards high selective gas sensing property to acetone. J. Mater. Chem. A **2**, 18635–18643 (2014)

35. H. Su, L. Jing, K. Shi, C. Yao, H. Fu, Synthesis of large surface area $LaFeO_3$ nanoparticles by SBA-16 template method as high active visible photocatalysts. J. Nanopart. Res. **12**, 967–975 (2010)

36. Y.M. Zhang, J. Zhang, J.L. Chen, Z.Q. Zhu, J.Q. Liu, Improvement of response to formaldehyde at Ag–$LaFeO_3$ based gas sensors through incorporation of SWCNTs. Sens. Actuators B **195**, 509–514 (2014)

37. Y. Yuan, Z. Dong, Y. Li, Z. Lu, Y. Zhao, W. Bo, S. Han, Electrochemical properties of $LaFeO_3$–rGO composite. Prog. Nat. Sci. Mater. Int. **27**, 88–92 (2017)

38. Z. Dai, C.S. Lee, B.Y. Kim, C.H. Kwak, J.W. Yoon, H.M. Jeong, J.H. Lee, Honeycomb-like periodic porous $LaFeO_3$ thin film chemiresistors with enhanced gas-sensing performances. ACS Appl. Mater. Interfaces **6**(18), 16217–16226 (2014)

39. D. Kathiravan, B.R. Huang, A. Saravanan, Self-assembled hierarchical interfaces of ZnO nanotubes/graphene heterostructures for efficient room temperature hydrogen sensors. ACS Appl. Mater. Interfaces **9**, 12064–12072 (2017)

40. J. Liu, S. Li, B. Zhang, Y. Xiao, Y. Gao, Q. Yang, Y. Wang, G. Lu, Ultrasensitive and low detection limit of nitrogen dioxide gas sensor based on flower-like ZnO hierarchical nanostructure modified by reduced graphene oxide. Sens. Actuators B **249**, 715–724 (2017)

41. A. Taubert, F. Stange, Z. Li, M. Junginger, M. Neumann, A. Friedrich, CuO nanoparticles from the strongly ILP tetrabutylammonium hydroxide: evaluation of the ethanol sensing activity. ACS Appl. Mater. Interfaces **4**, 791–795 (2012)

42. N. Sharma, H. Singh Kushwaha, S.K. Sharma, K. Sachdev, Fabrication of $LaFeO_3$ and rGO–$LaFeO_3$ thin film chemiresistors with enhanced gas-sensing performances—$LaFeO_3$ microspheres-based gas sensors for detection of NO_2 and CO. RSC Adv. **11**, 1297–1308 (2020)

43. F. Liu, X. Chu, Y. Dong, W. Zhang, W. Sun, L. Shen, Acetone gas sensors based on graphene–$ZnFe_2O_4$ composite prepared by solvothermal method. Sens. Actuators B **188**, 469–474 (2013)

44. I. Choudhuri, N. Patra, A. Mahata, R. Ahuja, B. Pathak, B–N@graphene: highly sensitive and selective gas sensor. J. Phys. Chem. C **119**, 24827–24836 (2015)